THE JOURNAL OF PHYSICAL CHEMISTRY C
A JOURNAL OF THE AMERICAN CHEMICAL SOCIETY

pubs.acs.org/JPCC Article

XANES Studies of Zinc Tin Oxide Films Deposited by Atomic Layer Deposition: Revealing Process-Structure Relationships for Amorphous Oxide Semiconductors

Published as part of The Journal of Physical Chemistry virtual special issue "Esther Sans Takeuchi Festschrift".

Orlando Trejo, Tae H. Cho, Sami Sainio, and Neil P. Dasgupta*

Cite This: https://doi.org/10.1021/acs.jpcc.2c05656 Read Online

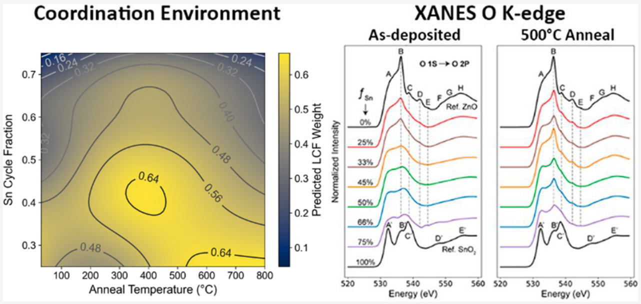

ABSTRACT: Amorphous oxide semiconductors have grown in technological relevance in displays, information technology, energy, and catalysis. Recent research efforts have converged on the need to develop design principles for the electronic structure of these materials. Here, we systematically vary the cation composition and annealing temperatures of zinc tin oxide films using atomic layer deposition (ALD) and study their process-structure relationships with synchrotron X-ray absorption near-edge spectroscopy (XANES). Measurements of the O K-edge, Sn M-edge, and Zn L-edge are analyzed with *ab initio* and nonlinear statistical modeling to understand the changes in geometric and electronic structure of the films. A key finding from this approach is the ability to measure the changes in the relative contribution of the Zn and Sn s orbitals to the density of states near the conduction band minimum. Furthermore, we identify and delineate critical process-structure design principles when working with amorphous oxide semiconductor (AOS) material systems: (1) use of complementary diffraction and absorption spectroscopy techniques to characterize the as-deposited coordination environment; (2) accounting for gradual and abrupt changes in coordination environment as a function of processing parameters (stoichiometry, annealing, etc.); (3) revealing and exploiting the relevant knowledge and interdependence of coordination environments, orbital hybridizations, the density of states, and band structures. In the future, this multimodal X-ray analysis and modeling framework can be applied to understand the process-structure relationships needed to optimize AOS performance in devices.

INTRODUCTION

Amorphous materials lack the long-range order characteristic of crystalline materials but possess short-range order that gives rise to a vast parameter space to design and optimize their properties. A particular family of amorphous materials with growing technological relevance are oxide semiconductors. For example, amorphous oxide semiconductors (AOS) are currently applied in industrial applications that incorporate amorphous In−Ga−Zn−O (a-IGZO) into flat-panel displays. In the research setting, there is a growing body of work on the custom design of amorphous oxides to enable next-generation technologies such as solid-state batteries, thin-film photovoltaics, flexible electronics, and neuromorphic computing.[1−6] Zinc tin oxide (ZTO) is a technologically relevant material under investigation for perovskite solar cells and thin-film transistors.[7−13] To accelerate efforts to control their functional properties and optimize device performance, an increased fundamental understanding of the complex process−structure−property relationships of AOS is needed.

Recent research efforts have provided an initial framework to understand the fundamental principles of AOS design and optimization.[14−17] An important theme is that amorphous materials can have short-range order that determines their properties. One way of describing this short-range order is through the polyhedra created by the metal atom and its coordinating oxygen atoms.[3,14] These metal−oxygen (M-O) polyhedra are the building blocks for AOS. Through systematic structural analysis and *ab initio* modeling, research groups have identified how the interconnection of polyhedra changes as a result of tuning material processing knobs such as composition.[18−20] Since the restructuring of M-O polyhedra depends on the material system (i.e., the composition and types of elements) and the synthesis conditions (e.g., solution, physical or chemical vapor deposition), it is necessary to develop understandings that are material and process specific.

Received: August 8, 2022
Revised: November 1, 2022

There is a need for systematic structural analysis of AOS to further develop the theory necessary to design and engineer complex AOS. A key challenge is to obtain large quantities of high-quality information on the structural information over a vast process parameter space. To address this need, researchers are combining laboratory characterization tools with synchrotron X-ray spectroscopy, specifically X-ray absorption spectroscopy (XAS). For example, Enman et al. used a combination of UV−vis spectrophotometry, XAS, and X-ray photoelectron spectroscopy (XPS) to characterize solution-processed amorphous metal oxides and provided a framework for the rational design of their electronic structure.[15]

In this study, we perform a multimodal analysis that combines XANES, X-ray diffraction (XRD), and *ab initio* modeling, to study ZTO thin films fabricated by ALD, followed by postdeposition annealing. The films were deposited using our recently developed ALD process, which allows for synthesis of ZTO thin films with atomically precise tuning of composition, thickness, and conformality.[13] ALD presents advantages over solution-processed methods as it can yield pinhole-free and low impurity films with moderate deposition temperatures and vacuum pressures, and ALD can also be scaled over large surface areas without sacrificing uniformity. Furthermore, ALD enables the synthesis of amorphous materials with tunable properties, which can be subsequently modified with postdeposition annealing steps that modify the structure and properties.[13,21−23]

Despite these synthetic advantages, determining the amorphous local structure in ALD films is challenging. In a recent work, Young et al. investigated the atomic structure of amorphous ALD Al_2O_3 using high-energy X-ray diffraction and pair distribution function analysis.[24] The authors observed how the growth conditions result in Al−O bond length variations, Al vacancies, and local coordination environment distortions. This motivates the development of further methodologies to deepen our understanding of the local chemical environment in amorphous ALD films. For example, while ALD is often modeled as a cyclic and layered ABAB process of deposition steps, additional structural rearrangements occur as the deposited atoms locally reorganize and condense into the bulk film structure. To further probe these dynamic processes, XAS has emerged as a powerful technique to characterize subtle changes in the local geometric and electronic structure of ALD thin films.[25−30]

The complexity required to understand the properties of amorphous ALD films increases significantly when the film is composed of more than two elements.[11,13,31] For example, the local coordination of oxygen atoms in amorphous lithium borate-carbonate films deposited by ALD has been shown to influence Li^+ ionic conductivity.[4] Changes in deposition temperature affect the ratio of bridging to nonbridging oxygen atoms, which in turn determines the mobility of oxygen and lithium species within the film. In another example, the choice of Al precursor has been shown to influence the dispersion of dopants in Al-doped ZnO (AZO) films deposited by ALD, which results in a higher doping efficiency.[32] This was attributed to the differences in steric hindrances of the precursor ligands, which reduce local structural and electronic interactions between adjacent Al atoms in the ZnO matrix. Overall, a deeper fundamental understanding of the local atomic structure of multielement ALD films is necessary to design thin films for future applications.

To further establish the electronic structure design principle of AOS, we carried out a synchrotron XAS structural analysis of ALD ZTO thin films with systematic variation of the cation composition and annealing temperature. We collected the O K-, Sn M-, and Zn L-edge spectra to capture element-specific structural differences in ZTO films. We modeled the XANES spectra using *ab initio* multiple scattering calculations with FEFF9 to capture how the relative contributions of the projected density of states (PDOS) change with processing conditions. Furthermore, we applied nonlinear statistical modeling methods to create a landscape that captures the gradual and abrupt changes in the coordination environment of the Zn−O and Sn−O polyhedra. The results of this study illustrate how multimodal X-ray analysis, combined with first-principles modeling, can improve our understanding of local structure in AOS thin films and enable rational design of ternary ALD films by leveraging its atomically precise control of synthesis.

■ METHODS

Atomic Layer Deposition. Atomic layer deposition (ALD) was performed using a custom-built, cross-flow thermal ALD station.[33] All depositions were performed at a substrate temperature of 200 °C. Zinc tin oxide was deposited using a supercycle approach with subsets of subcycles comprising different numbers of ZnO and SnO_2 cycles. ZnO was deposited using diethylzinc (DEZ), and SnO_2 was deposited using tetrakis (dimethylamino) tin(IV) (TDMASn) as the metal precursor. The oxidant used for both depositions was H_2O. One cycle of the binary oxide within the supercycle consisted of a metal precursor pulse (0.05 s for DEZ and 0.20 s for TDMASn), Ar purge (30 s), H_2O pulse (0.10 s), and Ar purge (30 s). The Ar carrier gas flow rate was set at 10 sccm for all depositions. The base pressure of the system was 0.531 Torr at 10 sccm. The SnO_2 to ZnO cycle ratios were modified based on the relative number of binary oxide cycles within the supercycle (ex. for 45% SnO_2, one supercycle is comprised of 6 ZnO and 5 SnO_2 cycles). A 12 nm thick ALD ZTO film was used throughout the experiments to be consistent with our previous study.[13] After the deposition, the samples were annealed at 300 °C, 500 °C, or 800 °C in an ambient tube furnace environment. The temperature was ramped up over 1 h, held for 2 h, and then cooled at the room temperature.

Material Characterization and Modeling. X-ray diffraction (XRD) analysis was performed using a Rigaku Smartlab X-ray Diffractometer at a grazing incidence of 1° for 2θ from 20° to 70°. The samples were prepared on a Si (100) substrate with a size of 20 mm × 20 mm. XRD data were analyzed using the PDXL 2 software to determine the phases that were present in the film as a function of the postdeposition annealing temperature and SnO_2 cycle fractions.

The samples were characterized at beamline 10−1 at the Stanford Synchrotron Radiation Lightsource (SSRL), with a probing area of approximately 200 μm × 1000 μm. For the XAS measurements, multiple total electron yield (TEY) spectra were gathered for the O K-, Sn M3-, and Zn L2,3-edges. Total fluorescence yield (TFY) spectra were also collected for oxygen, which agreed with the TEY data sets. The XAS spectra were aligned, averaged, and normalized using the Athena analysis package.

Theoretical XANES spectra were generated using the FEFF9 code based on Green's function multiple-scattering theory.[34] The atomic structure information for ZnO (mp-2133) and

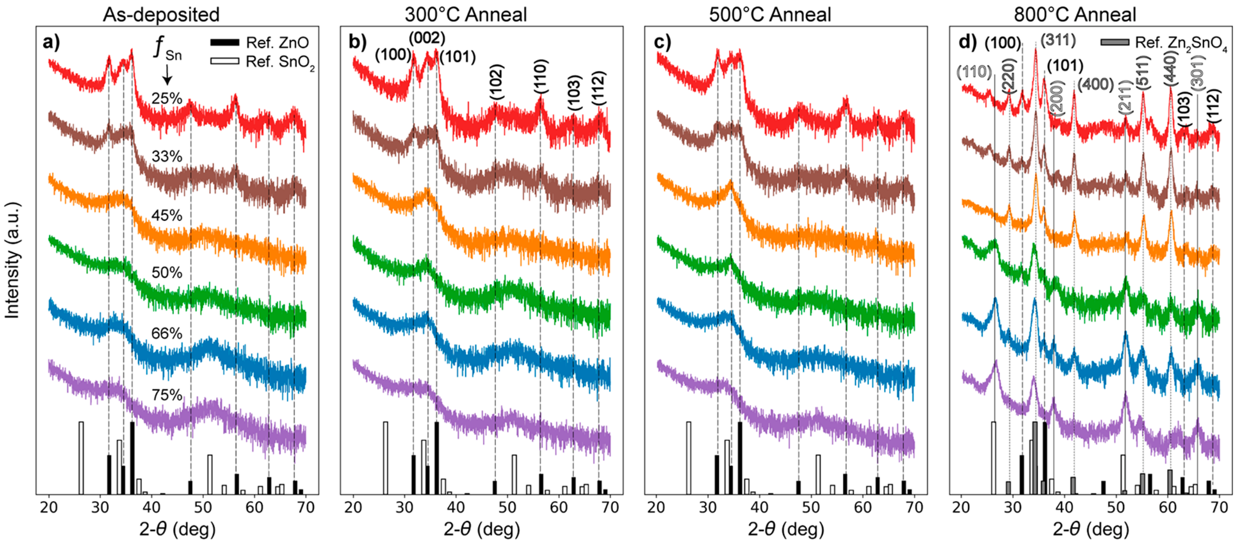

Figure 1. XRD Analysis. The XRD spectra of (a) as-deposited and (b-d) annealed ZTO films with different Sn cycle fractions.

SnO_2 (mp-856) was obtained from the Materials Project and the corresponding O−K spectra was compared.[35]

RESULTS AND DISCUSSION

In the following paragraphs, we discuss how XANES spectra can be used to capture the structural changes in ZTO as a function of film composition and annealing temperature. We then correlate these trends with changes in the density of states of the conduction band.

To fabricate ternary ZTO films by ALD, the Sn cycle fraction, f_{Sn}, is defined as the percentage of Sn precursor cycles used in the deposition sequence, and the Sn elemental fraction, c_{Sn}, is defined as the Sn atomic composition in ZTO film (eqs 1 and 2, respectively). For example, a f_{Sn} of 50% indicates that for every Sn cycle, there is one corresponding Zn cycle, while a f_{Sn} of 25% represents that for every Sn cycle there are three Zn cycles.

$$f_{sn} = \frac{SnO_{2_{cycles}}}{SnO_{2_{cycles}} + ZnO_{cycles}} \tag{1}$$

$$c_{sn} = \frac{Sn_{atomic\ percent}}{Sn_{atomic\ percent} + Zn_{atomic\ percent}} \tag{2}$$

In this study, we analyzed ALD ZTO films with f_{Sn} values of 25%, 33%, 45%, 50%, 66%, and 75%. The corresponding elemental compositions of the ZTO films was analyzed using XPS and is shown in Figure S3. As we have previously demonstrated, post-deposition annealing of ALD ZTO films results in an enhancement of the field-effect mobility in thin-film transistor (TFT) devices.[13] Therefore, to study the influence of annealing on the local chemical structure, the films were subsequently annealed at 300 °C, 500 °C, and 800 °C. For the reference samples, we measured samples of binary ALD oxide films composed of ZnO (f_{Sn} of 0%) and SnO_2 (f_{Sn} of 100%), which were both annealed at 500 °C.

XRD Analysis. We carried out XRD measurements to gauge the degree of long-range crystallinity in the ZTO films (Figure 1). From the XRD measurements, ZTO films with Sn cycle fractions from 45% to 75% that were annealed at temperatures up to 500 °C show little-to-no crystalline structure. Peaks can be observed for the wurtzite ZnO phase in the films deposited with 25% and 33% Sn cycle fractions under all of the annealing conditions. At 800 °C, there is a clear presence of rutile SnO_2 for Sn cycle fractions between 50% and 75%. Similarly, there are well-defined Zn_2SnO_4 diffraction peaks for Sn cycle fractions 25% to 45%.

It is known that as-deposited ALD ZnO films are polycrystalline.[36] Wurtzite ZnO peaks in ZTO films are also expected with lower Sn cycle fractions (more Zn rich).[13,21,22] In the observed ZTO films that exhibit ZnO peaks, the XRD spectra suggest that there are regions in the ZTO films where there is well-defined ZnO ordering.[22] The remainder of the film is an amorphous matrix of Sn and O atoms with additional Zn atoms that were not integrated into the crystalline regions. In ZTO films with Sn cycle fractions of 45% and higher, the absence of crystalline peaks from XRD indicates that the higher presence of Sn disrupts the local wurtzite ZnO structure, resulting in an amorphous material.

After annealing at 300 and 500 °C, we observe subtle changes in the samples from the as-deposited conditions. The ZTO films remain largely amorphous, with evidence of crystalline ZnO regions in films with Sn cycle fractions of 25% and 33%. A slight sharpening can be observed in the region of the (002) ZnO peak for the 45% ZTO film, as the annealing temperature increases. This sharpening may indicate the onset of ZnO crystallinity.[21] However, after increasing the annealing temperature to 800 °C, the predominant crystalline phase in the 45% sample is Zn_2SnO_4. We also note that the location of the (311) peak Zn_2SnO_4 phase is close to the ZnO (002) peak, and thus, it is also possible that the peak sharpening in this region is associated with the emergence of the Zn_2SnO_4 phase rather than ZnO. To decouple these possibilities, the XANES spectra at the O K-edge and Zn L-edge (which will be discussed in the subsequent sections) indicate that any structured short-range order in the vicinity of O and Zn atoms is associated with ZnO coordination. This demonstrates the power of the multimodal diffraction and XAS approach presented herein to deepen our understanding of the complex structure of multielement ALD films with high degrees of disorder.

After annealing at 800 °C, all of the ZTO films exhibit crystallinity, with varying contributions from the ZnO, SnO_2,

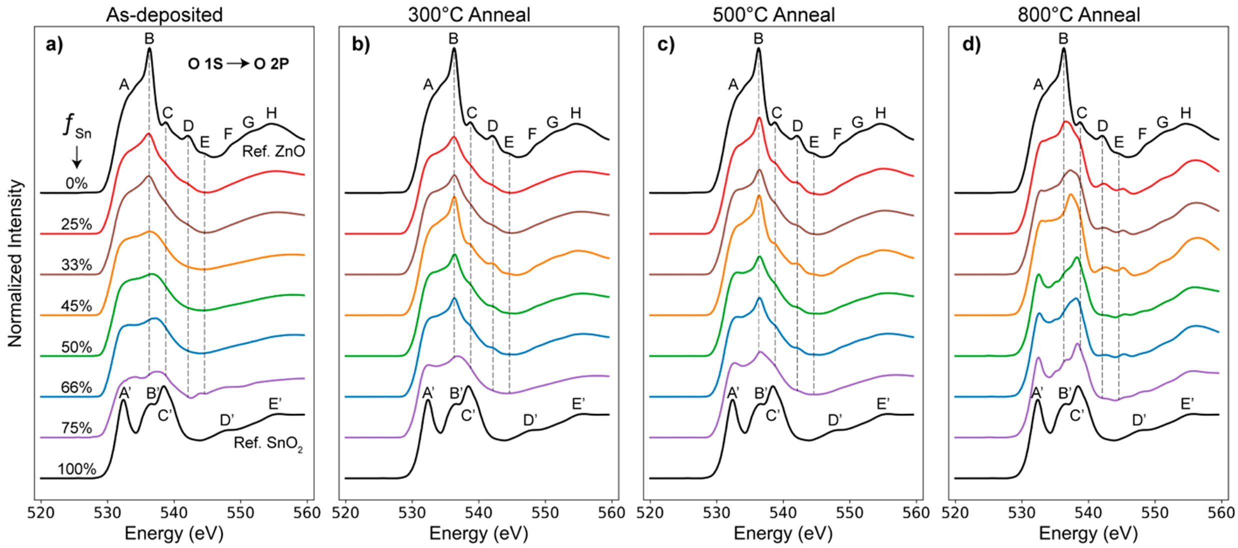

Figure 2. O K-edge. The O K-edge spectra of reference ZnO, reference SnO$_2$, and (a) as-deposited and (b-d) annealed ZTO films with different Sn cycle fractions. The main features for the ZnO (f_{Sn} = 0%) and SnO$_2$ (f_{Sn} = 100%) reference spectra are labeled. The reference spectra in all panels correspond to 500 °C annealed ALD ZnO and SnO$_2$ films. Dashed lines provide a way to visually compare the ZTO samples to the first four features in the ZnO reference.

and Zn$_2$SnO$_4$ phases. The XRD spectra for the ZTO films that were deposited with lower Sn cycle fractions (25% to 45%) indicate the presence of the Zn$_2$SnO$_4$ phase. The 33% and 45% ZTO films exhibit primarily the (220), (311), (222), (400), (551), and (440) peaks of Zn$_2$SnO$_4$, with minimal evidence of the other phases. The 25% ZTO film indicates the presence of ZnO in addition to Zn$_2$SnO$_4$, as can be seen by the well-defined (100) ZnO peak. The remaining ZTO films predominantly exhibit the SnO$_2$ phase, with small Zn$_2$SnO$_4$ contributions for the 50% and 66% films.

Overall, the XRD spectra can capture the absence or the presence of long-range ordering of the ZTO films with varying Sn cycle fractions and annealing conditions. The observed trends are in line with previous XRD work on ZTO films with varying Sn to Zn stoichiometries and annealing temperatures.[13] It is also clear that the XRD spectra do not capture the subtle changes in local structure that give rise to the tunable electronic properties of ZTO within the amorphous regime. Therefore, it is necessary to use complementary characterization techniques sensitive to nonperiodic structure. Toward this goal, we carried out XANES studies on the O-K, Sn-M, and Zn-L edges to unveil subtle changes in the local coordination environment in ZTO films, which will influence the electronic structure and charge transport properties of the AOS.

O K-edge. In metal oxides, the O K-edge captures transitions from the O 1s orbitals to hybridized O 2p orbitals in the conduction band.[34] In the case of ZnO, the O 2p orbitals are hybridized mostly with the Zn 4s and 4p orbitals.[26,27,37−41] A similar form of O 2p hybridization takes place in the SnO$_2$ conduction band with Sn 5s and 5p orbitals.[42] For a multication material like ZTO, there is a varying degree of hybridization between the O 2p, Zn 4s/4p, and Sn 5s/5p states as a function of cation composition and local coordination structure.[42−44]

Figure 2 shows the O K-edge spectra for all of the analyzed ZTO films, as well as the reference ZnO and SnO$_2$ samples. In Figure 2a, as-deposited ZTO samples exhibit broadened and smoothened features that indicate the presence of both amorphous structure and oxygen vacancies.[26,27,38] The as-deposited 25% and 33% Sn cycle fraction samples start to exhibit the C, D, and E features of ZnO as the Zn cycle ratio increases. This increasing similarity to ZnO is a result of the higher concentration of Zn in the ZTO films, which gives rise to increased local ordering since ZnO films deposited by ALD crystallize as-deposited.[36,45] We note that the features in the D and E regions of as-deposited f_{Sn} = 75% SnO$_2$ sample are artifacts due to data acquisition issues.

The data for ZTO samples that were annealed at 300 and 500 °C are plotted in Figure 2b and c, respectively. From the XANES spectra, it is evident that there are structural changes present in all of the annealed ZTO samples when compared to the as-deposited films. After annealing at 300 and 500 °C, the samples ranging from 25% to 66% exhibit a ZnO B feature, while the 75% samples have a profile that resembles the SnO$_2$ reference. Given the coordination environment of ZnO, the B feature primarily arises from bonding between the O 2p and Zn 4s orbitals, as captured in the ZnO O 2p, Zn 4s, and Zn 4p DOS (Figure S6).[46] A nonintuitive observation is that the 45% samples have the closest resemblance to the ZnO reference. Intuitively, one would expect that the samples with the highest Zn concentrations would exhibit the closest similarity to the ZnO reference. However, in both the 300 and 500 °C samples, the 45% O K-edge spectra have the largest linear combination fit with the ZnO O K-edge (Supporting Information Table 1). This illustrates that the relationships between processing parameters and local structure within the ALD films do not always vary monotonically, which we attribute to the local rearrangements of atoms within the film as the layer-by-layer ALD growth in a supercycle process dynamically evolves into a condensed ALD film. We further note that these atomic rearrangements occur at the local scale and are not driven by bulk diffusion because there are no significant concentration gradients throughout the film thickness, as has been previously shown by XPS depth profiling (Figure S3).

After annealing at 800 °C, there is an increased similarity between the ZTO films and the SnO$_2$ reference, especially for the 50%, 66%, and 75% samples. The 25%, 33%, and 45%

samples have a plateau feature that is in the region of the ZnO A feature. A change in the profile can be observed, including shifts to higher energies in the ZnO B feature. Additionally, there is an abrupt transition in structure from 45% to 50%. This is consistent with the XRD spectra of the 800 °C annealed films, where we also observe a deviation from the monotonic trends in phase percentage (further details in Supporting Information).

One potential reason for these non-monotonic trends may relate to the specific order of ALD cycles used in the process recipes (Table S2). When designing these ternary oxide ALD recipes, the binary ZnO and SnO_2 subsupercycles were intermixed in a manner that maximizes the homogeneity of cation incorporation, which was accomplished by minimizing the number of sequential deposition cycles of a single binary oxide within the recipe. We have previously demonstrated that this strategy results in the highest electron mobility in ALD ZTO films.[13] We further note that in the Zn-rich and Sn-rich compositions, the ALD recipes inevitably require multiple sequential depositions of the same binary oxide, which could influence the local coordination environment as the atoms relax into their final coordinates within the film. This is an inherent feature of ALD of ternary oxides, where the layer-by-layer growth sometimes necessitates repetition of similar binary subcycles. These factors may further contribute to the trends observed in the XANES spectra, where Zn-rich and Sn-rich compositions increasingly resemble the coordination environments of binary oxides. This highlights an important difference in ALD processing of multielement films compared to continuous processes such as CVD, solution processing, etc. In ALD, the sequential nature of layer-by-layer growth introduces new subtleties in the local coordination environment, which can lead to nonlinearities in the resulting film structure. These sudden changes in the XANES spectra highlight the sensitivity in process conditions in amorphous materials, which is an area of significant importance in the ALD field.[21,22,32,45,47,48]

In Supplementary Figure 1 (Figure S1), we plot the corresponding linear combination fittings (LCF) of the ZTO O K-edge spectra (Figure 2) as a function of f_{Sn} for the as-deposited and annealed conditions. The linear combination fits consist of finding the weighting values for the ZnO and SnO_2 spectra that can provide the best fit to the experimental spectra. As shown in Figure S1 and summarized in Table S1, the as-deposited samples follow the expected trends of larger ZnO weights for low f_{Sn} and smaller ZnO weights at higher f_{Sn}. After annealing at 300 and 500 °C, the monotonic trend flattens such that there is a more mixed characteristic in the linear combination fits across the various Sn cycle fractions. Additionally, there is an unexpected maximum ZnO resemblance at 45%. This maximum in ZnO characteristic is correlated with our TFTs having optimal mobility at 45% and 500 °C annealing, indicating that these non-monotonic trends in process-structure relationships have a direct impact on the electronic properties of the films.[13]

Figure 2 and Table S1 both summarize the LCF fits from Figure S1 in the Supporting Information. To map the local coordination environment of the oxygen atoms in ZTO as a function of Sn cycle fraction and annealing temperature, we created a contour plot using a neural network (NN) model to interpolate the ZnO LCF weights in Table S1. The NN model was constructed using a multilayer perceptron regressor consisting of three layers with 20 neurons in each layer, which enables us to capture the nonlinear changes across the spectra as the function of processing conditions.[49] The resulting 2-D map in Figure 3 illustrates the coupled relationships between cation stoichiometry and thermal restructuring. According to the NN model, the maximum predicted ZnO resemblance occurs around f_{Sn} = 40% and at an annealing temperature of 400 °C, as well as at the lowest Sn cycle fractions and highest annealing temperatures. This level of analysis helps guide further material and device optimization.[50] For example, the data suggest that one could further optimize ZTO TFTs by exploring Sn cycle fractions between 30% and 50% and annealing temperatures between 300 and 500 °C.

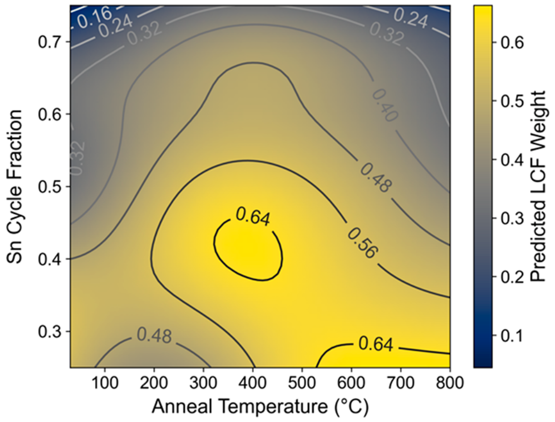

Figure 3. Two-dimensional O K-edge map. A contour plot constructed using a neural network regressor on the ZnO LCF weights of the O K-edge spectra.

Sn M-edge. In SnO_2 films, the Sn $M_{4,5}$-edge is associated with transitions from the Sn 3d states to the hybridized Sn 5p and 5f orbitals in the conduction band.[51−55] The M_4 region (spanning the E′, F′, and G′ peaks) corresponds to excitations from the Sn $3d_{3/2}$ orbitals, while the M_5 region (spanning the B′, C′, and D′ peaks) is a result of Sn $3d_{5/2}$ excitations. Undercoordinated Sn atoms, typically due to dangling bonds, oxygen vacancies, and Sn interstitials in SnO_x films, give rise to resonance peaks at ∼486 eV (indicated in Figure 4 as A′) and ∼494 eV (not explicitly indicated in Figure 4 due to the overlap with the bulk D′ peak).[51−57]

Figure 4 shows the Sn $M_{4,5}$-edge spectra for the ZTO films and the SnO_2 reference. The as-deposited ZTO films exhibit broad and smooth features that indicate amorphous structure and distinctive resonances from undercoordinated Sn atoms in the A′ region and near the D′ region. As expected, the as-deposited samples exhibit increasing A′ and D′ intensities as the Sn cycle fraction increases. The B′ and the E′ features around 490 and 497 eV are similar in shape and position throughout all the samples whereas features C′ and F′ are missing from the as-deposited ZTO films.

Annealing at 300 °C suppresses the undercoordinated Sn resonances in the A′ and near the D′ regions. There is still evidence of undercoordinated Sn atoms in the 66% and 75% Sn cycle fraction samples. Given the presence of undercoordinated Sn, in the future, it may be interesting to explore annealing in O_2-rich environments, which has previously been suggested to decrease the O vacancy content in ZTO films.[58] From Figure 4b, we infer that the annealing results in more stoichiometric SnO_2 octahedra, but they remain intercon-

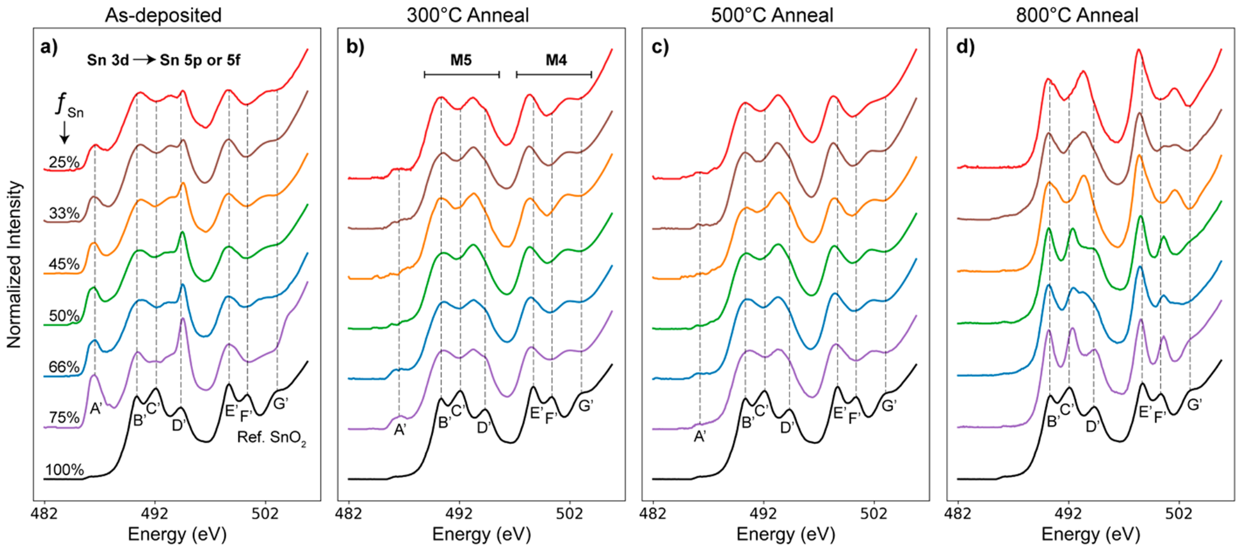

Figure 4. Sn $M_{4,5}$-edge. The Sn $M_{4,5}$-edge spectra of reference SnO_2 and (a) as-deposited and (b-d) annealed ZTO films with different Sn cycle fractions. The main features for the SnO_2 (f_{Sn} = 100%) reference are labeled, with the additional A′ due to undercoordinated Sn atoms in the as-deposited ZTO samples. The reference spectra in all panels correspond to 500 °C annealed SnO_2 films. Dashed lines provide a way to visually compare the ZTO samples to the six main features of the SnO_2 reference.

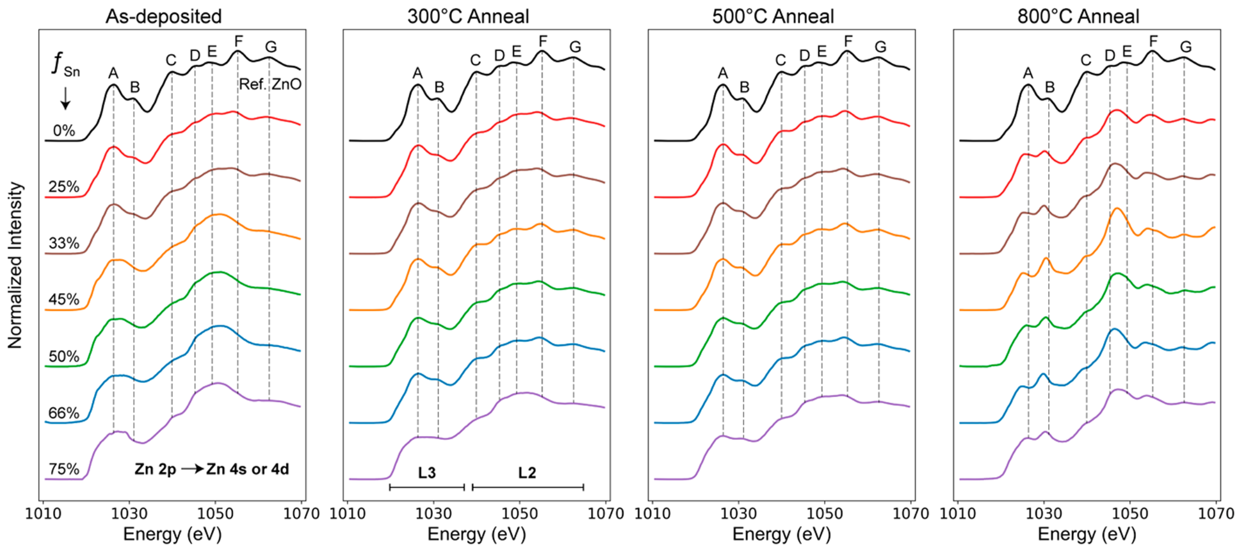

Figure 5. Zn $L_{2,3}$-edge. The Zn $L_{2,3}$-edge spectra of (a) as-deposited and (b-d) annealed ZTO films with different Sn cycle fractions. The main features for the ZnO (f_{Sn} = 0%) reference are labeled. The reference spectra in all panels correspond to 500 °C annealed ZnO films. Dashed lines provide a way to visually compare the ZTO samples to the seven main features of the ZnO reference.

nected in an amorphous manner. The two broad features at the B′ position and in between the C′ and D′ regions confirm that the amorphous structure in the M_5 edge is distinct from the SnO_2 reference, which is characterized by three peaks. Similarly, in the M_4 edge, the features at F′ and G′ are missing in the ZTO samples annealed at 300 °C.

After annealing at 500 °C, the ZTO films remain amorphous and have fewer unsaturated Sn atoms (Figure 4c). For the 25% to 45% samples, the second feature in the M_5 region (between C′ and D′) has a higher intensity (relative to the B′ peak) than in the corresponding 300 °C samples, which is likely due to more unoccupied Sn 5p states in the conduction band.[52] The M4 edges are similar across the 300 and 500 °C annealed samples.

The most substantial differences among the samples occur after annealing at 800 °C. As expected, there is an increasing similarity to the SnO_2 reference with an increasing Sn cycle ratio. 50%, 66%, and 75% Sn fraction samples have three distinct features in the M_5 region (B′, C′, and D′). In contrast, the 25%, 33%, and 45% samples have only two distinct features in the same energy region. In the M_4 edge region, the 50%, 66%, and 75% have E′ and F′ peaks, while the 75% is the only sample with a G′ shoulder. The 25%, 33%, and 45% have E′ peaks with features between the F′ and G′ regions.

The as-deposited samples have exhibited intensities at the A′ and near the D′ regions. In previous studies, the A′ and D′ peaks are attributed to undercoordinated Sn at surfaces of nanostructured SnO_x (e.g., nanoparticles or nanoribbons).[21,22,59−61] Therefore, given that our samples are thin films and ALD ZTO exhibits complex growth behavior, we suspect that the Sn atoms are also undercoordinated in as-deposited ALD ZTO. We thus conclude that based on the Sn

https://doi.org/10.1021/acs.jpcc.2c05656
J. Phys. Chem. C XXXX, XXX, XXX−XXX

Scheme 1. Conceptual Schematic of the Local Evolution in Coordination Environment and Crystallinity during Annealing

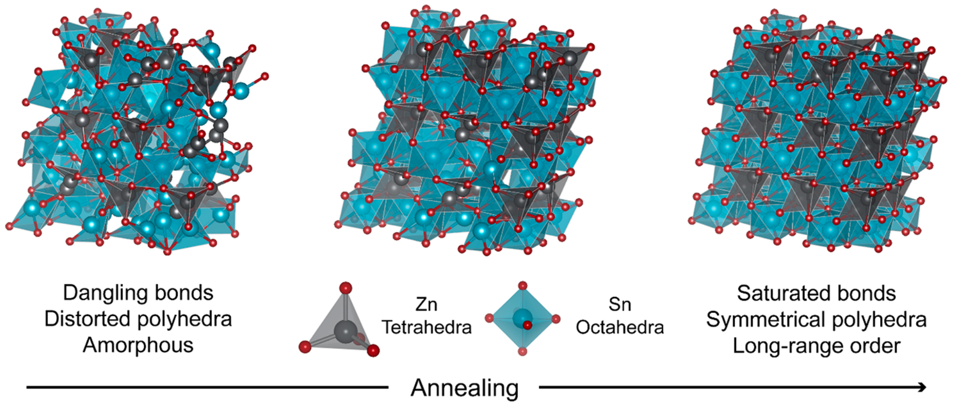

M edge spectra, Sn atoms throughout the films are undercoordinated, especially those near the surface. Since ALD SnO_2 grows amorphous at our deposition temperature of 200 °C and there is a monotonic increase in the A′ and D′ peaks with increasing Sn fraction, we also infer the presence of SnO_x polyhedra with dangling bonds and oxygen vacancies. Furthermore, we observe that post-deposition annealing reduces the presence of undercoordinated Sn atoms in the films (Figure 4b,c). This demonstrates the power of XANES to identify the changes in local coordination environment independent of changes in long-range order.

The M_5 region captures differences between the 25% to 45% samples and the 50% to 75% set when annealing from 300 °C and above. The 25% to 45% samples do not exhibit all three M5 features after annealing. The lack of these features suggests that the Sn−O coordination environment does not converge toward SnO_2 octahedra under the respective process conditions. In contrast, the 50% to 75% samples exhibit features at or near the A′, B′, and C′ regions. Therefore, the Sn coordination environment is converging toward the SnO_2 octahedra with higher Sn cycle fractions and annealing temperatures. A key takeaway from the Sn M_5 edge is that while the 45% and 50% samples are similar in composition, the as-deposited atomic structure and stoichiometry are sufficiently different to result in the phase divergence that is observed after annealing. Such phase differences with small changes in composition are the result of the high sensitivity of amorphous oxides to processing conditions and are critical to understand when designing AOS materials for device applications.[14]

Zn L-edge. In the ZnO sample, Zn $L_{2,3}$-edge arises from excitations between core Zn 2p orbitals to hybridized Zn 4s/4d states in the conduction band.[29,39−41,62−64] The hybridizations that yield the L_3 edge (peaks A and B) are from the Zn 4s orbitals at ∼1020 eV and the Zn 4d states above 1025 eV. The O 2p, Zn 4s, and Zn 4d DOS are plotted in Figure S7 to illustrate the orbital contributions to the Zn $L_{2,3}$-edge. Changes in the feature intensities and position of the L_3 features capture differences in the Zn coordination environment in multication materials.[64]

Figure 5 shows the Zn $L_{2,3}$-edge spectra for the ZTO films. Most of the as-deposited samples exhibit broadened and smoothed features that indicate an amorphous structure, while samples with Sn fractions of 25% and 33% more closely resemble the ZnO reference. Therefore, consistent with the O K-edge spectra, the as-deposited 25% and 33% Sn fraction samples are amorphous, but the Zn atoms are in coordination environments similar to ZnO tetrahedra.

After 300 °C annealing, the Zn L-edge spectra of the ZTO samples show all of the main features from the ZnO reference, with the exception of the 75% Sn cycle fraction sample. The development of these features indicates that the thermal treatment is restructuring the Zn coordination environment toward the ZnO tetrahedral symmetry. The 300 °C O K-edge spectra support this claim since the B feature of the O K-edge also appears for all samples except for the 75% film.

After increasing the annealing temperature to 500 °C, all of the ZTO films showed the ZnO L-edge features. In the 25% to 66% samples, the peaks became better-defined, while in the 75% Sn fraction sample, the features remained broad and smooth. In conjunction with the corresponding O K-edge spectra, we infer that the local ZnO structures for all cation compositions resemble the ZnO tetrahedra after annealing the ZTO films at 500 °C.

After 800 °C annealing, all of the ZTO Zn L-edge spectra deviate from the ZnO reference in a similar manner, where the main spectral changes occur in the A, B, D, and E regions. In the A and B ZTO peaks, there is a shift to lower energies, and the B feature shows a higher intensity than A. The D and E regions for ZTO samples appear to merge into one feature that falls between the D and E peaks of the ZnO reference. These differences in spectra, when compared to the ZnO reference, indicate new phases for the ZnO polyhedra. The trends in the Zn L-edge at 800 °C are further consistent with the new phases observed in the O K- and Sn M-edge spectra.

As can be seen by the XANES spectra and corroborated by the XRD patterns, there is a gradual shift from fully amorphous to crystalline structure as a function of Sn cycle ratio and annealing temperature, which is illustrated in a conceptual visualization in Scheme 1. The XANES spectra are able to distinctively capture the undercoordination of the Sn atoms and the distorted local structure around the Zn atoms of the as-deposited films. With annealing, the Sn atoms become fully coordinated and the Zn atoms start to adopt the ZnO tetrahedral local symmetry. The effects are more pronounced with increasing Zn content in the films. While most of the Sn atoms are fully coordinated after annealing at 500 °C, the Sn atoms are observed to be in the octahedral local structure until annealing at 800 °C for films with a higher Sn content. Given that the XANES spectra clearly capture the subtle changes in coordination and symmetry in the ZTO films with varying stoichiometries and annealing conditions, our next step will be

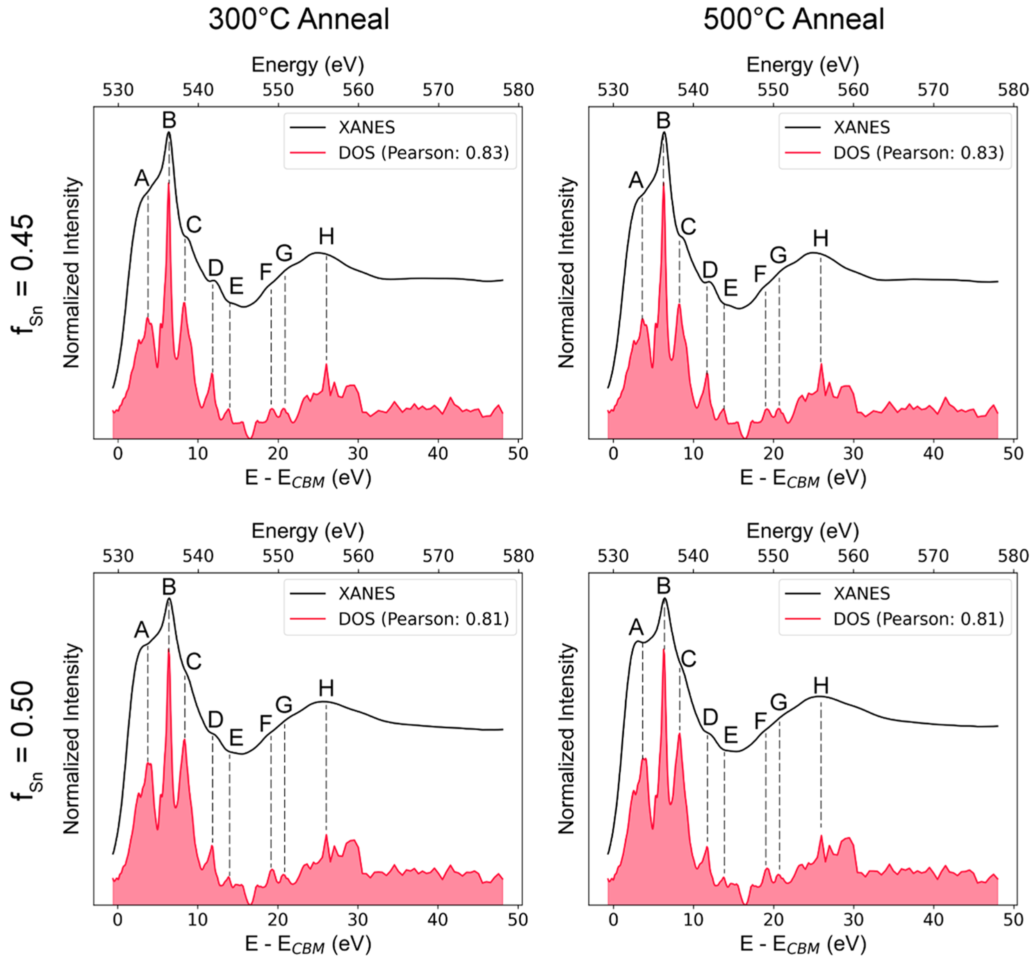

Figure 6. O 2p DOS. The O 2p DOS contribution in selected ZTO O K-edge spectra.

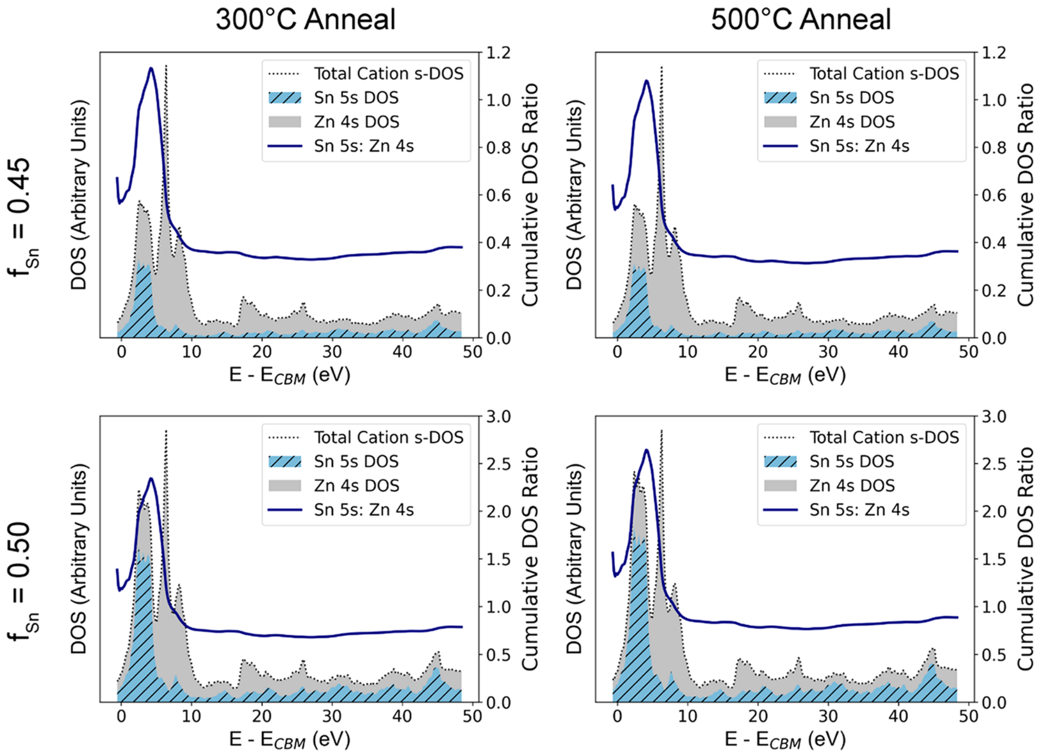

Figure 7. Cation DOS. The Zn 4s and Sn 5s DOS contribution in selected ZTO samples.

https://doi.org/10.1021/acs.jpcc.2c05656
J. Phys. Chem. C XXXX, XXX, XXX−XXX

to use this knowledge to determine the implications of the electronic structure evolution for charge transport.

Density of States. The band structure of amorphous semiconductors can be understood by considering the interactions of molecular clusters, where long-range order is not necessary for the formation of bands.[65] In AOS, the valence band is typically composed of O 2p states, while metal *ns* states make up the conduction band.[1,66] Carrier transport in amorphous metal oxides is determined by the wave function overlap of metal s-orbitals.[67] Therefore, the contributions of the cation s orbitals in the conduction band minimum (CBM) influence the mobility in materials like ZTO.

To understand how the orbital contributions change in the ZTO conduction band as a function of process conditions, the projected DOS for O 2p, Zn 4s, and Sn 5s orbitals of selected ZTO samples are plotted in Figures 6 and 7. The DOS were calculated using FEFF9.

In Figure 6, the O 2p DOS are plotted, along with the corresponding O K-edge spectra for the 300 and 500 °C annealed ZTO samples with Sn cycle fractions of 45% and 50%. We chose to focus on these annealing conditions and compositions because they have been previously shown to result in TFT performance with high mobilities, with the 45% composition to leading to the highest mobilities.[13] The ZTO O 2p DOS was calculated using a linear combination of the O 2p DOS for ZnO and SnO_2, given the corresponding weights from Table S1. For all the plotted samples, the Pearson correlation coefficient is above 0.8, indicating that the unoccupied O 2p DOS in ZTO correlates strongly with the O K-edge spectra. Therefore, a linear combination of the ZnO and SnO_2 O 2p orbitals is a valid approximation to the O 2p states in ZTO.

In particular, in the region between 530 and 540 eV, a clear peak in intensity is visible in both the DOS and XANES spectra, which allows for alignment to the B peak in the ZnO reference. For this set of samples, the emergence of the A, C, and D peaks in the XANES spectra clearly align with the DOS. There are also small features in the DOS that correspond with the E, F, G, and H XANES features.

To understand how the metal *ns* orbitals are changing in the conduction band of ZTO, we plot the linear combinations of the simulated Zn 4s and Sn 5s DOS using the weights from Table S1, as shown in Figure 7. The energy region below 8 eV of the spectrum represents the DOS band near the ZTO conduction band minimum (CBM). There are clear trends in the *ns* DOS in this band near the CBM as a function of Sn cycle fraction and annealing temperatures.

To quantify these trends, we also overlay the ratio between the cumulative Sn 5s DOS to the cumulative Zn 4s DOS. For the 45% samples, the contribution between the Sn 5s and Zn 4s is almost 1:1 for the DOS band near the CBM (less than 8 eV from the CBM). In contrast, the band near the CBM in the 50% samples is mostly composed of Sn 5s, reaching a cumulative Sn 5s: Zn 4s of ~2.5. This metal ns DOS analysis implies that charge transport in the 45% sample likely occurs evenly across the Zn and Sn ns orbitals, while charge transport in the 50% sample mostly occurs in Sn 5s orbitals. Furthermore, there are changes between annealing conditions for both sets of samples for a given Sn cycle fraction, more notably in the 50% samples, which capture how the metal *ns* orbital contribution to the states near the CBM is not solely a function of composition, but is also affected by the local coordination environment.

Through the use of LCF fitting values, it is possible to confirm that the corresponding linear combinations of the DOS represent the O K-edge spectra. By using these same weights to compare the contribution of the Zn and Sn outermost s orbitals, we observe how the relative Zn and Sn contributions markedly change between the 45% and 50% samples. These results suggest that optimal charge transport in amorphous ZTO is achieved when the Zn atoms are closer to their local ZnO symmetry, while Sn atoms are in more distorted local environments and when the coordination between Zn and Sn polyhedra enables a balanced contribution of the metal s states to the CBM. Therefore, through the lens of the XANES spectra, it is possible to see how the composition and annealing temperature tune the relative contribution of the metal s orbitals of the CBM and the degree to which the Sn and Zn atoms are coordinated and adopt local symmetry. This approach can be extended to fundamentally understand the impact of annealing under O_2-rich or -lean environments, which may influence the coordination environment and O vacancies in the ALD ZTO film, as well as intermixing the anion species in multinary amorphous semiconductors.

CONCLUSIONS

In this study, we collected synchrotron XANES spectra from O K-, Sn M-, and Zn L-edges for ALD ZTO thin films. From the XANES measurements, we were able to capture changes in the local coordination environment of the films from as-deposited to annealed conditions. These changes were further understood by performing complementary XRD analysis. The ALD ZTO films are amorphous as deposited with distorted cation-oxygen polyhedra. After annealing, the Zn−O polyhedra start moving toward resembling the ZnO local structure, while the Sn−O polyhedra remain more amorphous with respect to the Sn−O polyhedra in SnO_2. From modeling of the DOS, it is shown how the relative contribution of cation ns orbitals in the CBM can be tuned with composition and annealing.

This work has implications for enabling materials by design, such as multielement semiconductors by ALD. By capturing how local order evolves in amorphous materials, it is possible to design complex thin films with custom orbital contributions in the electronic structure. Systematically exploring the design space of AOS is necessary to exploit their vast properties for energy-efficient and high-performance devices.

The soft XAS of the O K-, Sn M-, and Zn-L edges provide sufficient information to track the local coordination environment as amorphous ZTO films transition into crystalline films as a function of composition and annealing. One can then build models based on the spectral trends to see how the materials morph and evolve over the process window. This understanding can in turn be used to approximate how the cation s orbital contributions to the CBM and the respective polyhedra symmetry can be tuned by varying the process knobs. By understanding the process-structure relationships and subtle variations in atomic arrangements, we can predict new process states and model the electronic structure, which is imperative for the optimization of more complex amorphous metal oxide semiconductors.

ASSOCIATED CONTENT

Supporting Information

The Supporting Information is available free of charge at https://pubs.acs.org/doi/10.1021/acs.jpcc.2c05656.

Summary of the linear combination fits and predicted vs actual MLP plots; Elemental composition of ZTO films; Summary of cycle ratios with corresponding ZnO and SnO_2 per 1 ALD supercycle; XRD of binary ZnO and SnO_2; Summary of elemental composition of deposited ZTO films; Density of states for ZnO (PDF)

■ AUTHOR INFORMATION

Corresponding Author

Neil P. Dasgupta − *Department of Mechanical Engineering and Department of Materials Science & Engineering, University of Michigan, Ann Arbor, Michigan 48109, United States;* orcid.org/0000-0002-5180-4063; Email: ndasgupt@umich.edu

Authors

Orlando Trejo − *Department of Mechanical Engineering, University of Michigan, Ann Arbor, Michigan 48109, United States*

Tae H. Cho − *Department of Mechanical Engineering, University of Michigan, Ann Arbor, Michigan 48109, United States*

Sami Sainio − *Department Stanford Synchrotron Radiation Lightsource, SLAC National Accelerator Laboratory, Menlo Park, California 94025, United States; Microelectronics Research Unit, Faculty of Information Technology and Electrical Engineering, University of Oulu, 90570 Oulu, Finland*

Complete contact information is available at: https://pubs.acs.org/10.1021/acs.jpcc.2c05656

Notes

The authors declare no competing financial interest.

■ ACKNOWLEDGMENTS

This material is based upon work supported by the National Science Foundation under Grant No. 1727918. Portions of this work were performed at the Lurie Nanofabrication Facility and Michigan Center for Materials Characterization, which are supported by the College of Engineering at University of Michigan. O.T. acknowledges the support of the Department of Energy (DOE) EERE Postdoctoral Research Award. Use of the Stanford Synchrotron Radiation Lightsource, SLAC National Accelerator Laboratory, is supported by the U.S. Department of Energy, Office of Science, Office of Basic Energy Sciences under contract no. DE-AC02-76SF00515. This project has received funding from the European Union's Horizon 2020 research and innovation programme under the Marie Skłodowska-Curie grant agreement No 841621. The authors would also like to thank Dr. Christopher R. Allemang and Dr. Rebecca L. Peterson for providing expertise in Zn−Sn−O for the beamline proposal and comments on the manuscript, and acknowledge Dr. Fritz Prinz and Dr. Jan Torgersen group members for helping coordinate sample transfer between University of Michigan and SLAC.

■ REFERENCES

(1) Yu, X.; Marks, T. J.; Facchetti, A. Metal Oxides for Optoelectronic Applications. *Nat. Mater.* **2016**, *15* (4), 383−396.

(2) Zhou, N.; Kim, M.-G.; Loser, S.; Smith, J.; Yoshida, H.; Guo, X.; Song, C.; Jin, H.; Chen, Z.; Yoon, S. M.; Freeman, A. J.; Chang, R. P. H.; Facchetti, A.; Marks, T. J. Amorphous Oxide Alloys as Interfacial Layers with Broadly Tunable Electronic Structures for Organic Photovoltaic Cells. *Proc. Natl. Acad. Sci. U.S.A.* **2015**, *112*, 7897.

(3) Yan, S.; Abhilash, K. P.; Tang, L.; Yang, M.; Ma, Y.; Xia, Q.; Guo, Q.; Xia, H. Research Advances of Amorphous Metal Oxides in Electrochemical Energy Storage and Conversion. *Small* **2018**, 1804371.

(4) Kazyak, E.; Chen, K. H.; Davis, A. L.; Yu, S.; Sanchez, A. J.; Lasso, J.; Bielinski, A. R.; Thompson, T.; Sakamoto, J.; Siegel, D. J.; et al. Atomic Layer Deposition and First Principles Modeling of Glassy Li3BO3-Li2CO3 Electrolytes for Solid-State Li Metal Batteries. *J. Mater. Chem. A* **2018**, *6* (40), 19425−19437.

(5) Shen, C. K.; Chaurasiya, R.; Chen, K. T.; Chen, J. S. Synaptic Emulation via Ferroelectric P(VDF-TrFE) Reinforced Charge Trapping/Detrapping in Zinc-Tin Oxide Transistor. *ACS Appl. Mater. Interfaces* **2022**, *14* (14), 16939−16948.

(6) Schlupp, P.; Schein, F.-L.; Wenckstern, H.; Grundmann, M. All Amorphous Oxide Bipolar Heterojunction Diodes from Abundant Metals. *Adv. Electron. Mater.* **2015**, 1−5, DOI: 10.1002/aelm.201400023.

(7) Eperon, G. E.; Leijtens, T.; Bush, K. A.; Prasanna, R.; Green, T.; Wang, J. T.-W.; McMeekin, D. P.; Volonakis, G.; Milot, R. L.; May, R.; et al. Perovskite-Perovskite Tandem Photovoltaics with Optimized Band Gaps. *Science (80-.).* **2016**, *354* (6314), 861−864.

(8) Bush, K. A.; Palmstrom, A. F.; Yu, Z. J.; Boccard, M.; Cheacharoen, R.; Mailoa, J. P.; McMeekin, D. P.; Hoye, R. L. Z.; Bailie, C. D.; Leijtens, T.; et al. 23.6%-Efficient Monolithic Perovskite/Silicon Tandem Solar Cells With Improved Stability. *Nat. Energy* **2017**, *2* (4), 17009.

(9) Xu, J.; Boyd, C. C.; Yu, Z. J.; Palmstrom, A. F.; Witter, D. J.; Larson, B. W.; France, R. M.; Werner, J.; Harvey, S. P.; Wolf, E. J.; et al. Triple-Halide Wide-Band Gap Perovskites with Suppressed Phase Segregation for Efficient Tandems. *Science* **2020**, *367* (6482), 1097−1104.

(10) Cho, T. H.; Farjam, N.; Allemang, C. R.; Pannier, C. P.; Kazyak, E.; Huber, C.; Rose, M.; Trejo, O.; Peterson, R. L.; Barton, K.; et al. Area-Selective Atomic Layer Deposition Patterned by Electrohydrodynamic Jet Printing for Additive Manufacturing of Functional Materials and Devices. *ACS Nano* **2020**, *14* (12), 17262−17272.

(11) Hu, W.; Peterson, R. L. Charge Transport in Solution-Processed Zinc Tin Oxide Thin Film Transistors. *J. Mater. Res.* **2012**, *27* (17), 2286−2292.

(12) Lahr, O.; Bar, M. S.; von Wenckstern, H.; Grundmann, M. All-Oxide Transparent Thin-Film Transistors Based on Amorphous Zinc Tin Oxide Fabricated at Room Temperature: Approaching the Thermodynamic Limit of the Subthreshold Swing. *Adv. Electron. Mater.* **2020**, *6* (10), 2000423.

(13) Allemang, C. R.; Cho, T. H.; Trejo, O.; Ravan, S.; Rodríguez, R. E.; Dasgupta, N. P.; Peterson, R. L. High-Performance Zinc Tin Oxide TFTs with Active Layers Deposited by Atomic Layer Deposition. *Adv. Electron. Mater.* **2020**, *6*, 2000195.

(14) Medvedeva, J. E.; Buchholz, D. B.; Chang, R. P. H. Recent Advances in Understanding the Structure and Properties of Amorphous Oxide Semiconductors. *Adv. Electron. Mater.* **2017**, *3* (9), No. 1700082.

(15) Enman, L. J.; Kast, M. G.; Cochran, E. A.; Pledger, E.; Stevens, M. B.; Boettcher, S. W. Transition-Metal-Incorporated Aluminum Oxide Thin Films: Toward Electronic Structure Design in Amorphous Mixed-Metal Oxides. *J. Phys. Chem. C* **2018**, *122* (25), 13691−13704.

(16) Wahila, M. J.; Lebens-Higgins, Z. W.; Butler, K. T.; Fritsch, D.; Treharne, R. E.; Palgrave, R. G.; Woicik, J. C.; Morgan, B. J.; Walsh, A.; Piper, L. F. J. Accelerated Optimization of Transparent, Amorphous Zinc-Tin-Oxide Thin Films for Optoelectronic Applications. *APL Mater.* **2019**, *7* (2), 022509.

(17) Sallis, S.; Butler, K. T.; Quackenbush, N. F.; Williams, D. S.; Junda, M.; Fischer, D. A.; Woicik, J. C.; Podraza, N. J.; White, B. E.; Walsh, A. Origin of Deep Subgap States in Amorphous Indium

Gallium Zinc Oxide: Chemically Disordered Coordination of Oxygen. *Appl. Phys. Lett.* **2014**, *104* (23), 232108.

(18) Srivastava, J.; Nahas, S.; Bhowmick, S.; Gaur, A. Electronic Structure and Transport in Amorphous Metal Oxide and Amorphous Metal Oxynitride Semiconductors. *J. Appl. Phys.* **2019**, *126* (12), 125702.

(19) Triana, C. A.; Araujo, C. M.; Ahuja, R.; Niklasson, G. A.; Edvinsson, T. Disentangling the Intricate Atomic Short-Range Order and Electronic Properties in Amorphous Transition Metal Oxides. *Sci. Rep.* **2017**, *7* (1), 1−12.

(20) Nahas, S.; Gaur, A.; Bhowmick, S. First Principles Prediction of Amorphous Phases Using Evolutionary Algorithms. *J. Chem. Phys.* **2016**, *145* (1), 014106.

(21) Mullings, M. N.; Hägglund, C.; Tanskanen, J. T.; Yee, Y.; Geyer, S.; Bent, S. F. Thin Film Characterization of Zinc Tin Oxide Deposited by Thermal Atomic Layer Deposition. *Thin Solid Films* **2014**, *556*, 186−194.

(22) Tanskanen, J. T.; Hagglund, C.; Bent, S. F. Correlating Growth Characteristics in Atomic Layer Deposition with Precursor Molecular Structure: The Case of Zinc Tin Oxide. *Chem. Mater.* **2014**, *26*, 2795.

(23) Kazyak, E.; Shin, M.; Lepage, W. S.; Cho, T. H.; Dasgupta, N. P. Molecular Layer Deposition of Li-Ion Conducting "Lithicone" Solid Electrolytes. *Chem. Commun.* **2020**, *56* (99), 15537−15540.

(24) Young, M. J.; Bedford, N. M.; Yanguas-Gil, A.; Letourneau, S.; Coile, M.; Mandia, D. J.; Aoun, B.; Cavanagh, A. S.; George, S. M.; Elam, J. W. Probing the Atomic-Scale Structure of Amorphous Aluminum Oxide Grown by Atomic Layer Deposition. *ACS Appl. Mater. Interfaces* **2020**, *12* (20), 22804−22814.

(25) Trejo, O.; Roelofs, K. E.; Xu, S.; Logar, M.; Sarangi, R.; Nordlund, D.; Dadlani, A. L.; Kravec, R.; Dasgupta, N. P.; Bent, S. F.; et al. Quantifying Geometric Strain at the PbS QD-TiO2 Anode Interface and Its Effect on Electronic Structures. *Nano Lett.* **2015**, *15* (12), 7829−7836.

(26) Dadlani, A. L.; Trejo, O.; Acharya, S.; Torgersen, J.; Petousis, I.; Nordlund, D.; Sarangi, R.; Schindler, P.; Prinz, F. B. Exploring the Local Electronic Structure and Geometric Arrangement of ALD Zn(O,S) Buffer Layers Using X-Ray Absorption Spectroscopy. *J. Mater. Chem. C* **2015**, *3* (47), 12192−12198.

(27) Dadlani, A. L.; Acharya, S.; Trejo, O.; Prinz, F. B.; Torgersen, J. ALD Zn(O,S) Thin Films' Interfacial Chemical and Structural Configuration Probed by XAS. *ACS Appl. Mater. Interfaces* **2016**, *8* (23), 14323−14327.

(28) Torgersen, J.; Acharya, S.; Dadlani, A. L.; Petousis, I.; Kim, Y.; Trejo, O.; Nordlund, D.; Prinz, F. B. Relating Electronic and Geometric Structure of Atomic Layer Deposited BaTiO3 to Its Electrical Properties. *J. Phys. Chem. Lett.* **2016**, *7* (8), 1428−1433.

(29) Dadlani, A.; Acharya, S.; Trejo, O.; Nordlund, D.; Peron, M.; Razavi, J.; Berto, F.; Prinz, F. B.; Torgersen, J. Revealing the Bonding Environment of Zn in ALD Zn(O,S) Buffer Layers through X-Ray Absorption Spectroscopy. *ACS Appl. Mater. Interfaces* **2017**, *9* (45), 39105−39109.

(30) Trejo, O.; Dadlani, A. L.; De La Paz, F.; Acharya, S.; Kravec, R.; Nordlund, D.; Sarangi, R.; Prinz, F. B.; Torgersen, J.; Dasgupta, N. P. Elucidating the Evolving Atomic Structure in Atomic Layer Deposition Reactions with in Situ XANES and Machine Learning. *Chem. Mater.* **2019**, *31* (21), 8937−8947.

(31) Bitter, S.; Schlupp, P.; Bonholzer, M.; Von Wenckstern, H.; Grundmann, M. Influence of the Cation Ratio on Optical and Electrical Properties of Amorphous Zinc-Tin-Oxide Thin Films Grown by Pulsed Laser Deposition. *ACS Comb. Sci.* **2016**, *18* (4), 188−194.

(32) Wu, Y.; Potts, S. E.; Hermkens, P. M.; Knoops, H. C. M.; Roozeboom, F.; Kessels, W. M. M. Enhanced Doping Efficiency of Al-Doped ZnO by Atomic Layer Deposition Using Dimethylaluminum Isopropoxide as an Alternative Aluminum Precursor. *Chem. Mater.* **2013**, *25* (22), 4619−4622.

(33) Dasgupta, N. P.; MacK, J. F.; Langston, M. C.; Bousetta, A.; Prinz, F. B. Design of an Atomic Layer Deposition Reactor for Hydrogen Sulfide Compatibility. *Rev. Sci. Instrum.* **2010**, *81* (4), 044102.

(34) Rehr, J. J.; Kas, J. J.; Vila, F. D.; Prange, M. P.; Jorissen, K. Parameter-Free Calculations of X-Ray Spectra with FEFF9. *Phys. Chem. Chem. Phys.* **2010**, *12*, 5503−5513.

(35) Jain, A.; Ong, S. P.; Hautier, G.; Chen, W.; Richards, W. D.; Dacek, S.; Cholia, S.; Gunter, D.; Skinner, D.; Ceder, G. Commentary: The Materials Project: A Materials Genome Approach to Accelerating Materials Innovation. *APL Mater.* **2013**, *1* (1), 011002.

(36) Bielinski, A. R.; Kazyak, E.; Schlepütz, C. M.; Jung, H. J.; Wood, K. N.; Dasgupta, N. P. Hierarchical ZnO Nanowire Growth with Tunable Orientations on Versatile Substrates Using Atomic Layer Deposition Seeding. *Chem. Mater.* **2015**, *27* (13), 4799−4807.

(37) Dong, C. L.; Persson, C.; Vayssieres, L.; Augustsson, A.; Schmitt, T.; Mattesini, M.; Ahuja, R.; Chang, C. L.; Guo, J. H. Electronic Structure of Nanostructured ZnO from X-Ray Absorption and Emission Spectroscopy and the Local Density Approximation. *Phys. Rev. B - Condens. Matter Mater. Phys.* **2004**, *70* (19), 1−5.

(38) Zhang, S.; Du, Y.; Li, H.; Chu, W.; Li, J.; Yan, W.; Wei, S.; Yan, C.; Wu, Z. Evidence of Matrix Lattice Distortion in Zn1-XCoxO Nanocrystals. *J. Phys. Chem. C* **2009**, *113* (11), 4263−4269.

(39) Cho, D. Y.; Kim, J. H.; Na, K. D.; Song, J.; Hwang, C. S.; Park, B. G.; Kim, J. Y.; Min, C. H.; Oh, S. J. Spectroscopic Evidence for Limited Carrier Hopping Interaction in Amorphous ZnO Thin Film. *Appl. Phys. Lett.* **2009**, *95* (26), 261903.

(40) Hu, Q. C.; Ding, K.; Zhang, J. Y.; Yan, F. P.; Pan, D. M.; Huang, F.; Chiou, J. W. On the Variations of Optical Property and Electronic Structure in Heavily Al-Doped ZnO Films during Double-Step Growth Process. *Appl. Phys. Lett.* **2014**, *104* (2), 21913.

(41) Bikowski, A.; Zajac, D. A.; Vinnichenko, M.; Ellmer, K. Evidence for the AlZn-Oi Defect-Complex Model for Magnetron-Sputtered Aluminum-Doped Zinc Oxide: A Combined X-Ray Absorption near Edge Spectroscopy, X-Ray Diffraction and Electronic Transport Study. *J. Appl. Phys.* **2019**, *126* (4), 45106.

(42) Kim, H. W.; Lee, E.; Kim, D. H.; Seong, S.; Moon, S. Y.; Shin, Y. J.; Baik, J.; Shin, H. J.; Kang, J. S. Soft X-Ray Absorption and Photoemission Spectroscopy Study of Semiconductor Oxide Nanoparticles for Dye-Sensitized Solar Cell: ZnSnO3 and Zn2SnO4. *Solid State Commun.* **2016**, *236*, 32−36.

(43) Kapilashrami, M.; Kronawitter, C. X.; Törndahl, T.; Lindahl, J.; Hultqvist, A.; Wang, W.-C.; Chang, C.-L.; Mao, S. S.; Guo, J. Soft X-Ray Characterization of Zn1−xSnxOy Electronic Structure for Thin Film Photovoltaics. *Phys. Chem. Chem. Phys.* **2012**, *14* (29), 10154.

(44) Lee, J.; Cho, D. Y.; Jung, J.; Ki Kim, U.; Ho Rha, S.; Seong Hwang, C.; Choi, J. H. Theoretical and Experimental Studies on the Electronic Structure of Crystalline and Amorphous ZnSnO3 Thin Films. *Appl. Phys. Lett.* **2013**, *102* (24), 242111.

(45) Dasgupta, N. P.; Neubert, S.; Lee, W.; Trejo, O.; Lee, J. R.; Prinz, F. B. Atomic Layer Deposition of Al-Doped ZnO Films: Effect of Grain Orientation on Conductivity. *Chem. Mater.* **2010**, *22* (16), 4769−4775.

(46) Frati, F.; Hunault, M. O. J. Y.; De Groot, F. M. F. Oxygen K-Edge X-Ray Absorption Spectra. *Chem. Rev.* **2020**, *120*, 4056−4110.

(47) Mackus, A. J. M.; Schneider, J. R.; Macisaac, C.; Baker, J. G.; Bent, S. F. Synthesis of Doped, Ternary, and Quaternary Materials by Atomic Layer Deposition: A Review. *Chem. Mater.* **2019**, *31* (4), 1142−1183.

(48) Wu, Y.; Giddings, A. D.; Verheijen, M. A.; Macco, B.; Prosa, T. J.; Larson, D. J.; Roozeboom, F.; Kessels, W. M. M. Dopant Distribution in Atomic Layer Deposited ZnO:Al Films Visualized by Transmission Electron Microscopy and Atom Probe Tomography. *Chem. Mater.* **2018**, *30* (4), 1209−1217.

(49) Barupal, D. K.; Fiehn, O. Generating the Blood Exposome Database Using a Comprehensive Text Mining and Database Fusion Approach. *Environ. Health Perspect.* **2019**, *127* (9), 097008.

(50) Cao, B.; Adutwum, L. A.; Oliynyk, A. O.; Luber, E. J.; Olsen, B. C.; Mar, A.; Buriak, J. M. How to Optimize Materials and Devices via

Design of Experiments and Machine Learning: Demonstration Using Organic Photovoltaics. *ACS Nano* **2018**, *12*, 7434−7444.

(51) Baumann, T. F.; Kucheyev, S. O.; Gash, A. E.; Satcher, J. H. Facile Synthesis of a Crystalline, High-Surface-Area SnO2 Aerogel. *Adv. Mater.* **2005**, *17* (12), 1546−1548.

(52) Kucheyev, S. O.; Baumann, T. F.; Sterne, P. A.; Wang, Y. M.; Van Buuren, T.; Hamza, A. V.; Terminello, L. J.; Willey, T. M. Surface Electronic States in Three-Dimensional SnO2 Nanostructures. *Phys. Rev. B - Condens. Matter Mater. Phys.* **2005**, *72* (3), 35404 DOI: 10.1103/PhysRevB.72.035404.

(53) Zhou, X. T.; Heigl, F.; Murphy, M. W.; Sham, T. K.; Regier, T.; Coulthard, I.; Blyth, R. I. R. Time-Resolved x-Ray Excited Optical Luminescence from SnO2 Nanoribbons: Direct Evidence for the Origin of the Blue Luminescence and the Role of Surface States. *Appl. Phys. Lett.* **2006**, *89* (21), 213109.

(54) Zhou, J. G.; Fang, H. T.; Maley, J. M.; Ko, J. Y. P.; Murphy, M.; Chu, Y.; Sammynaiken, R.; Sham, T. K. An X-Ray Absorption, Photoemission, and Raman Study of the Interaction between SnO2 Nanoparticle and Carbon Nanotube. *J. Phys. Chem. C* **2009**, *113* (15), 6114−6117.

(55) Bolotov, V. V.; Nesov, S. N.; Korusenko, P. M.; Povoroznyuk, S. N. Transformation of the Electronic Structure of the SnO2 − x/MWCNT Nanocomposite under High-Vacuum Annealing Conditions. *Phys. Solid State* **2014**, *56* (9), 1899−1903.

(56) Zhou, X. T.; Zhou, J. G.; Murphy, M. W.; Ko, J. Y. P.; Heigl, F.; Regier, T.; Blyth, R. I. R.; Sham, T. K. The Effect of the Surface of SnO2 Nanoribbons on Their Luminescence Using X-Ray Absorption and Luminescence Spectroscopy. *J. Chem. Phys.* **2008**, *128* (14), 144703.

(57) Bolotov, V. V.; Korusenko, P. M.; Nesov, S. N.; Povoroznyuk, S. N.; Shelyagin, R. V. XANES and XPS Studies of Processes Initiated by High-Vacuum Annealing in SnOx/MWCNT Composite Layers. *Phys. Solid State* **2013**, *55* (6), 1289−1293.

(58) Cho, S.; Yang, J. H.; Oh, J. G.; Cho, S. H.; Hwang, C. S.; Jang, J.; Nam, S. The Role of Oxygen in Dramatically Enhancing the Electrical Properties of Solution-Processed Zn-Sn-O Thin-Film Transistors. *J. Mater. Chem. C* **2017**, *5* (26), 6521−6526.

(59) Lindahl, J.; Hagglund, C.; Watjen, J. T.; Edoff, M.; Torndahl, T. The Effect of Substrate Temperature on Atomic Layer Deposited Zinc Tin Oxide. *Thin Solid Films* **2015**, *586*, 82−87.

(60) Hägglund, C.; Grehl, T.; Tanskanen, J. T.; Yee, Y. S.; Mullings, M. N.; Mackus, A. J. M.; MacIsaac, C.; Clemens, B. M.; Brongersma, H. H.; Bent, S. F. Growth, Intermixing, and Surface Phase Formation for Zinc Tin Oxide Nanolaminates Produced by Atomic Layer Deposition. *J. Vac. Sci. Technol. A Vacuum, Surfaces, Film.* **2016**, *34* (2), No. 021516.

(61) Mackus, A. J. M.; Macisaac, C.; Kim, W. H.; Bent, S. F. Incomplete Elimination of Precursor Ligands during Atomic Layer Deposition of Zinc-Oxide, Tin-Oxide, and Zinc-Tin-Oxide. *J. Chem. Phys.* **2017**, *146* (5), No. 052802.

(62) Horwat, D.; Jullien, M.; Capon, F.; Pierson, J. F.; Andersson, J.; Endrino, J. L. On the Deactivation of the Dopant and Electronic Structure in Reactively Sputtered Transparent Al-Doped ZnO Thin Films. *J. Phys. D. Appl. Phys.* **2010**, *43* (13), No. 132003.

(63) Yuste, M.; Escobar Galindo, R.; Caretti, I.; Torres, R.; Snchez, O. Influence of the Oxygen Partial Pressure and Post-Deposition Annealing on the Structure and Optical Properties of ZnO Films Grown by Dc Magnetron Sputtering at Room Temperature. *J. Phys. D. Appl. Phys.* **2012**, *45* (2), 25303−25314.

(64) Caretti, I.; Yuste, M.; Torres, R.; Sánchez, O.; Jiménez, I.; Escobar Galindo, R. Coordination Chemistry of Titanium and Zinc in Ti (1-x)Zn 2xO 2 ($0 \leq x \leq 1$) Ultrathin Films Grown by DC Reactive Magnetron Sputtering. *RSC Adv.* **2012**, *2* (7), 2696−2699.

(65) Adler, D. Chemistry and Physics of Amorphous Semiconductors. *J. Chem. Educ.* **1980**, *57* (8), 560−564.

(66) Nomura, K.; Ohta, H.; Takagi, A.; Kamiya, T.; Hirano, M.; Hosono, H. Room-Temperature Fabrication of Transparent Flexible Thin-Film Transistors Using Amorphous Oxide Semiconductors. *Nature* **2004**, *432* (7016), 488−492.

(67) Srivastava, J.; Nahas, S.; Bhowmick, S.; Gaur, A. Electronic Structure and Transport in Amorphous Metal Oxide and Amorphous Metal Oxynitride Semiconductors. *J. Appl. Phys.* **2019**, *126* (12), 125702.